

Jae Won Lee
James D. Huggins
Wayne J. Book

George W. Woodruff School of Mechanical Engineering
Georgia Institute of Technology
Atlanta, GA 30332

From Proceedings of the
1988 American Control Conf.
June 15-17, 1988, Atlanta,
Georgia, pp 1021-1028

ABSTRACT

A large experimental lightweight manipulator would be useful for material handling, for welding, or for ultrasonic inspection of a large structure such as an airframe. The flexible parallel link mechanism is designed for high rigidity without increasing weight. This constrained system is analyzed by singular value decomposition of the constraint Jacobian matrix. This paper presents a verification of the modeling using the assumed mode method. Eigenvalues and eigenvectors of the linearized model are compared to the measured system natural frequencies and their associated mode shapes. The modeling results for large motions are compared to the time response data from the experiments. The hydraulic actuator are also verified.

1. Introduction

A large, two link flexible manipulator designated RALF (Robotic Arm, Large and Flexible) that has been constructed in the Flexible Automation Laboratory at Georgia Institute of Technology is shown in Fig. 1.1. The structure consists of two ten foot long links made of aluminum tubing actuated by hydraulic cylinders. The outer link is driven using a parallel link mechanism. This large manipulator can effectively reach a much larger workspace than traditional robots. Such a configuration would be useful for material handling, welding, or ultrasonic inspection of large structures such as airframes. Using lightweight design concepts, it is possible to construct large manipulators with low power consumption and high load to weight ratios.

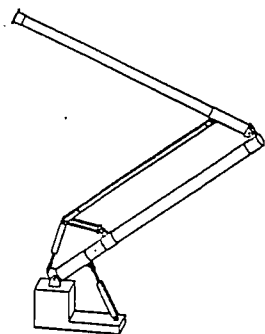


Figure 1.1 RALF
(Robotic Arm, Large and Flexible)

In a conventional serial link mechanism, the outer link is driven by a motor attached at the tip of the inner link. The weight of the second motor must be carried by the first link. This increases the torque and power the first motor must provide. Especially noticeable in lightweight arms is the increased structural vibration due to the weight and reaction torque of the second actuator. To

reduce these interactive effects, the rigidity of lower link should be increased. An alternative to serial link robot construction is utilization of a closed kinematic chain, such as a parallel mechanism. Although a variety of research topics on serial link mechanisms can be found in robotics literature, the research on constrained systems such as closed chain mechanisms is rare and is mostly concerned with rigid manipulators. The parallel mechanism with rigid links has a simple relationship between its generalized coordinates. However, a parallel mechanism with flexible links has a complicated nonlinear algebraic constraint equation. To solve these mixed differential and nonlinear algebraic equations, an efficient and stable computational method should be used.

The special case when the closed chains are parallelograms was studied extensively by Asada [1], Megahed [2] and Luh [3] derived the equations of motion by the Lagrange and Newton-Euler methods, respectively. However, a computationally efficient algorithm for inverse dynamics of closed chain mechanisms is required. Chung [4] derived the equations of motion of lightweight arms with flexible parallel links, but assumed that the actuating link and the inner link had the same mode shapes so that constraints need not be considered.

Solving a mixed set of differential equations of motion (dimension n) and nonlinear algebraic equations of kinematic constraint (dimension m) is difficult and the methods are not yet fully understood. Nikravesh [5] reviewed three integration algorithms for this purpose. These are the direct integration method, the constraint violation stabilization method, and the generalized coordinate partitioning method. The first two methods are sensitive to initial conditions on the system. In the third method, the generalized coordinates are partitioned into independent (dimension $n - m$) and dependent (dimension m) sets. Numerical integration is carried out for independent generalized coordinates. Constraint equations are solved for dependent generalized coordinates. The choice of the correct initial conditions is not critical and the dimension of the equations of motion is minimum.

When partitioning generalized coordinates, an important consideration is the choice of independent generalized coordinates. An arbitrary selection of independent generalized coordinates often results in ill-conditioned matrices. Wehage [6] identified independent generalized coordinates using LU partitioning of the constraint Jacobian matrix. Mani [7] and Singh [8] used singular value decomposition. Kim [9] used QR decomposition. A unique and accurate independent generalized coordinates can be obtained from the last two methods. Furthermore, singular value decomposition is a more robust algorithm than the QR method and has a variety of applications in linear control systems.

This paper presents a verification of the modeling using the assumed mode method. First, the results from a linearization of the model about zero velocity are compared to measured system frequencies and their associated mode shapes. Next, the modeling results for large motions are compared to the time response data from the experiments. Finally, the hydraulic dynamics are also verified.

2. Derivation of constrained dynamic equations

2.1 Constrained Equations of Motion

To analyze a closed kinematic chain system, one joint of the flexible parallel link is virtually cut to form an open tree structure. An equation describing the constraint force at the point where the cut was made is then required. For this manipulator, the cut is made at the joint between the actuating link and the upper link. Lagrange's equations and the assumed mode method is used for deriving the equations of motion of this open tree flexible structure. In order to describe the motion, the reference frame is defined as shown in Figure 2.1. The absolute position vectors of an arbitrary point on each link are described by the following:

$$\vec{r}_i = \vec{R}_i + \vec{U}_{ri} + \vec{U}_{fi} \quad (2.1)$$

where \vec{R}_i is the position vector of the origin of the reference body with respect to the global frame, \vec{U}_{ri} is the undeformed position vector, and \vec{U}_{fi} is the elastic deflection vector. \vec{U}_{fi} is composed of a linear combination of an admissible shape function, Ψ , multiplied by time dependant modal coordinates:

$$\vec{U}_{fi}(x, t) = \sum_{j=1}^n \Psi_{ij}(x) q_{fij}(t) \quad (2.2)$$

Assuming that the amplitude of the higher modes of flexible links are much smaller than the amplitudes of the first two modes, the system can be truncated with n equal to 2.

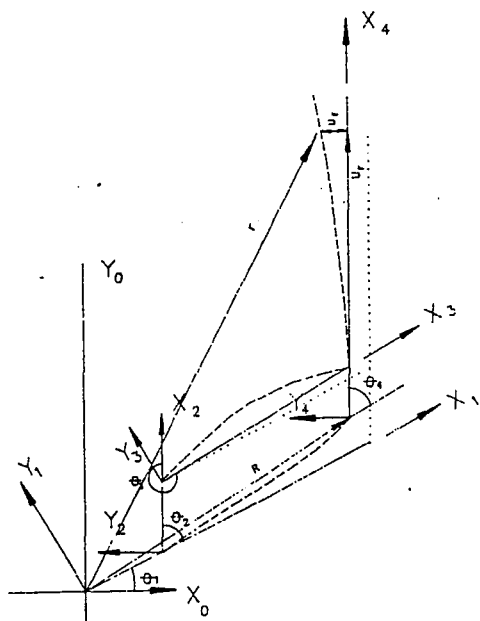


Figure 2.1
Coordinate Systems of Assumed Modes Model

The kinetic energy, T_i , of each element is obtained from the velocity vector of the infinitesimal volume:

$$T_i = \frac{1}{2} \rho \int \dot{\vec{r}}_i \cdot \dot{\vec{r}}_i dV \quad (2.3)$$

The strain energy, which is stored in the flexible mode, can be attributed to the elastic stiffness, K_i , which is evaluated by integration over the length of the beam:

$$K_i = (EI)_i \int \Psi_{ij}''^2 dx \quad (2.4)$$

The potential energy, V_i , of each element is composed of the strain energy and gravity force:

$$V_i = \frac{1}{2} q_{fi}^T K_i q_{fi} \quad (2.5)$$

where E is Young's modulus of elasticity, and I is the area moment of inertia.

The governing dynamic equations for the system are derived through Lagrange's equations:

$$\frac{d}{dt} \left(\frac{\partial T}{\partial \dot{q}_j} \right) - \frac{\partial T}{\partial q_j} + \frac{\partial V}{\partial q_j} = Q_e \quad (2.6)$$

The algebraic complexity in applying Lagrange's equation can be overcome using a symbolic manipulation program (11). The open tree system is constrained by a set of nonlinear algebraic constraint equations. These constraint relations can be adjoined to equations (2.6) using Lagrangian multipliers. The resulting dynamic equations can be rewritten in partitioned form in terms of the rigid and flexible coordinates:

$$\begin{bmatrix} M_{rr} & M_{rf} \\ M_{fr} & M_{ff} \end{bmatrix} \begin{bmatrix} \ddot{q}_r \\ \ddot{q}_f \end{bmatrix} + \begin{bmatrix} 0 & 0 \\ 0 & K_{ff} \end{bmatrix} \begin{bmatrix} q_r \\ q_f \end{bmatrix} + \begin{bmatrix} \Phi_{qr} \\ \Phi_{qf} \end{bmatrix} \lambda = \begin{bmatrix} Q_r \\ Q_f \end{bmatrix} \quad (2.7)$$

where subscripts r and f denote rigid and flexible coordinates, q is the generalized coordinates vector, M is the generalized mass matrix, K is the elastic stiffness matrix, Φ_q is the constraint Jacobian matrix, λ is the unknown constraint force vector and Q is the generalized force vector including Coriolis, centrifugal and gravity forces. The m holonomic constraints are applied to the virtually cut joint as

$$\Phi(q) = 0 \quad (2.8)$$

or

$$\Phi_q(q) \dot{q} = 0 \quad (2.9)$$

where

$$\Phi_q = \frac{\partial \Phi}{\partial q} \quad (2.10)$$

The initial condition must be consistent with system constraints, therefore:

$$q(t_0) = q_0 \quad (2.11.a)$$

$$\dot{q}(t_0) = \dot{q}_0 \quad (2.11.b)$$

2.2 Singular Value Decomposition for Constrained Dynamic Analysis

The $m \times n$ constraint Jacobian matrix Φ_q with $m < n$ can be decomposed into the form

$$\Phi_q = U \Sigma V^T \quad (2.12)$$

or with proper partitioning [10]:

$$\Phi_q = [U_1 \ U_2] \begin{bmatrix} \Sigma_m & 0 \\ 0 & 0 \end{bmatrix} \begin{bmatrix} V_1^T \\ V_2^T \end{bmatrix} \quad (2.13)$$

where U_i and V_i are orthonormal bases for four fundamental subspaces. The Σ_m is equal to $\text{diag}(\sigma_1, \sigma_2, \dots, \sigma_m)$ where the σ_i 's are called the singular values of matrix Φ_q , ordered $\sigma_1 \geq \sigma_2 \geq \dots > 0$. The columns of U_i are the orthonormal eigenvectors of the symmetric matrix $\Phi_q^T \Phi_q$ and σ_i^2 are the corresponding eigenvalues. The columns of V_i are the orthonormal eigenvectors of the symmetric matrix $\Phi_q \Phi_q^T$. It is noticeable that V_2 is the null space of Φ_q which satisfies the following relation:

$$\Phi_q V_2 = 0 \quad (2.14)$$

and Φ_q^+ , called the pseudo inverse of Φ_q , is defined as

$$\Phi_q^+ = [V_1 \ V_2] \begin{bmatrix} \Sigma_m^{-1} & 0 \\ 0 & 0 \end{bmatrix} \begin{bmatrix} U_1^T \\ U_2^T \end{bmatrix} \quad (2.15)$$

Using the nullity of $\Phi_q V_2$, an algorithm which eliminates the constraint forces from the equations of motion can be developed. Premultiplication by V_2^T in equation (2.7) gives

$$V_2^T M \ddot{q} + V_2^T K q = V_2^T Q \quad (2.16)$$

since $\Phi_q V_2 = 0$. Because the dimension of equation (2.16) is $(n-m) \times n$, an additional equation is needed to get the solution. A new variable, z , is defined which is a constrained independent coordinate with dimension $n - m$. Then $V_2 \dot{z}$ is the homogeneous solution to equation (2.9). That is,

$$\dot{q} = V_2 \dot{z} \quad (2.17)$$

Geometrically, equation (2.17) is the projection of the velocity vector, \dot{q} , onto the tangent hyperplane of the constraint surface. Similarly, the time derivative of equation (2.9) gives

$$\Phi_q \ddot{q} = -(\Phi_q)_q \dot{q}^2 \quad (2.18)$$

Due to the nullspace of Φ_q , $V_2 \ddot{z}$ is also the homogeneous solution to equation (2.18). Then \ddot{q} can be written as

$$\ddot{q} = -\Phi_q^+ (\Phi_q)_q \dot{q}^2 + V_2 \ddot{z} \quad (2.19)$$

Physically, the first and second terms on the right hand side of equation (2.19) represent the normal and tangential accelerations, respectively. By integrating equation (2.17), q is expressed as

$$q = V_2 z + C \quad (2.20)$$

where the constant C is chosen as zero to satisfy the constraint equation. Hence, the following $n-m$ independent equations can be derived from equations (2.16), (2.17) and (2.19)

$$V_2^T M V_2 \ddot{z} + V_2^T K V_2 z = V_2^T Q + V_2^T M \Phi_q^+ (\Phi_q)_q (V_2 \dot{z})^2 \quad (2.21)$$

And q and \dot{q} are calculated using equations (2.20) and (2.17). These equations are used for the nonlinear dynamic simulation.

3. Natural Frequencies and Mode Shapes

Natural frequencies and mode shapes can be derived from a linearized equations of motion. Eigenvalues and eigenvectors are obtained from the equations of motion of the reduced equations (2.21) linearized about zero velocity.

$$V_2^T M V_2 \ddot{z} + V_2^T K V_2 z = 0 \quad (3.1)$$

Eigenvalues of (3.1) are the same as those of the constrained equation (2.7). Eigenvectors of the constrained system are derived by transforming those of (3.1) as

$$q = V_2 z \quad (3.2)$$

For numerical analysis, selection of mode shape functions is necessary and may greatly influence the results. Clamped - mass boundary conditions are assumed for the lower link mode shape. Clamped - free boundary conditions are used for the upper link and pin - pin boundary conditions are used for the actuating link.

In previous work [12], the natural frequencies were derived by flexible part of unconstrained equations:

$$M_{ff} \ddot{q} + K_{ff} q = 0 \quad (3.3)$$

But, more accurate results were obtained by considering that the lower link bending is affected by the actuating link's rigid motion. The constrained dynamics including the actuator link motion is needed. When the actuators are fixed, velocities of θ_1, θ_2 are zero. New constraint equations between θ_3, θ_4 and the elastic coordinates are needed. The elements of the mass matrix related to θ_1, θ_2 - the first and second columns and rows - are deleted. The dynamic equation can be rewritten as

$$\bar{V}_2^T \bar{M} \bar{V}_2 \ddot{z} + \bar{V}_2^T \bar{K} \bar{V}_2 z = 0 \quad (3.4)$$

From these equations, natural frequencies are calculated. Eigenvectors are obtained by transformation, $V_2 Z$. As shown in Table 3.1, the frequencies including the constraint are closer to the FEM results. The second natural frequencies of each link do not match the FEM results because only two modes are included in the assumed mode method.

The results derived by the assumed mode method are compared with FEM results - a simplified model and a detailed model - and experimental results in Fig. 3.1.

FEM	CONSTRAINED	UNCONSTRAINED
7.83	7.84	8.17
15.90	16.90	17.80
30.76	30.70	30.00
94.68	104.00	104.00
119.50	120.00	120.00
123.23	127.00	127.50

Table 3.1
Comparison of natural frequencies
between constrained and unconstrained equations

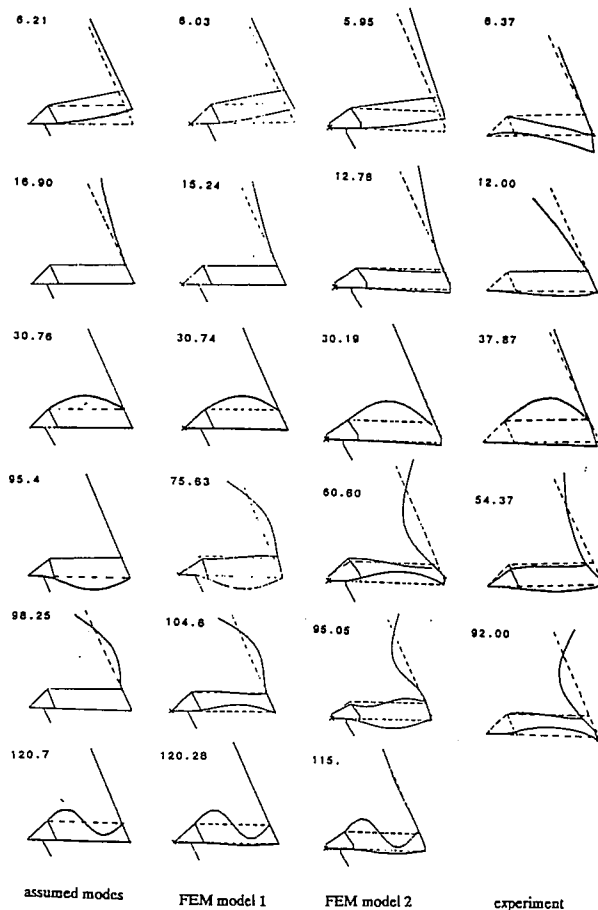


Figure 3.1
Comparison of mode shapes and
natural frequencies

The differences between the simplified FEM model (model 1) and the detailed FEM model (model 2) are bracket offsets. These offsets make some discrepancies between the simplified models (assumed mode model and FEM model 1) and actual models (FEM model 2 and experiment). The results of the experiment and FEM model 2 have similar mode shapes, but the frequencies are different because the damping in the actual system changes the boundary conditions of each link. To get more accurate results, the mode shape function of the assumed mode method should be computed from the FEM model.

4. Verification of Nonlinear Dynamics

4.1 Hydraulic Actuators: As a more detailed model of the manipulator was developed, a more accurate model of the hydraulic actuators was needed in order to accurately simulate the time response of the manipulator. Texts on modeling suggest that a third order model of hydraulic actuators is sufficient to describe their response up to their bandwidth even though the actual order is considerably higher. Two series of tests were made to measure the response of the cylinder position to a swept sine input. The tests included the open loop response, the closed loop response, and the closed loop stiffness response. The procedures used closely follow test methods outlined in Merritt [13].

The first series of tests were made with the actuator detached from the structure. A second series of tests were made with the actuators attached to the structure. A simple proportional only analog controller was used for the position loop control. A gain was chosen that would give a margin of stability and an appropriate bandwidth. This same gain was then used for all subsequent tests. When the digital controller was implemented on a Microvax II computer, an equivalent gain was chosen so that experimental results could be directly compared to the simulation results. Table 4.1 summarizes the results of these tests of the actuator.

	Joint 1 Actuator		Joint 2 Actuator	
	detached	attached	detached	attached
Open Loop Gain	127.8	79.6	72.2	51.7
Closed Loop Bandwidth	18.6 Hz	17.8 Hz	18.8 Hz	17.2 Hz
Gain Margin	8.6 db	10.6 db	7.5 db	14.6 db
Phase Margin	41.1 deg.	31.3 deg.	59.8 deg.	64.9 deg.

Table 4.1
Actuator frequency response data when
attached to and detached from the structure

Figure 4.1 shows the closed loop Bode plots of the response of the Joint 1 actuator to the swept sine input both when attached to and when detached from the structure. The similarity of these plots shows that the structure's influence on the response of the cylinder is small. That is, at the point of attachment, the manipulator follows the movement of the actuator very closely. Figure 4.2 shows the actual response of the cylinder verses the response computed from a third order curve fit. Again, the plots are very similar up to the bandwidth of the actuator. The Bode plots for the second joint actuators also show good agreement. The graphs are not included here for the sake of brevity.

4.2 Simulation Results vs. Experimental Results

Because the rigid body motion of the arm is dominated by hydraulic actuator dynamics, the time response of the rigid body motion of the arm can be derived from the frequency response of hydraulic actuator. From Bode plot curve fitting, hydraulic actuator dynamics can be approximated by a 3rd order system.

$$H_1(s) = \frac{1}{(S + 30.37)(S + 9.0 \pm j 16.5)} \quad (4.1.a)$$

$$H_2(s) = \frac{1}{(S + 33.57)(S + 21 \pm j 23.07)} \quad (4.1.b)$$

The calculated time response of this transfer function for a sine input and an arbitrary input function match with the measured

actual path as shown Fig. 4.3. The flexible motion of the arm is excited by acceleration of the rigid body. Flexible dynamics are derived from (2.16)

$$V_2^T M \ddot{q} + V_2^T K q = V_2^T Q \quad (2.16)$$

or

$$\begin{bmatrix} M_{rr} & M_{rf} \\ M_{fr} & M_{ff} \end{bmatrix} \begin{bmatrix} \ddot{q}_r \\ \ddot{q}_f \end{bmatrix} + \begin{bmatrix} 0 & K_{rf} \\ 0 & K_{ff} \end{bmatrix} \begin{bmatrix} q_r \\ q_f \end{bmatrix} = \begin{bmatrix} Q_r \\ Q_f \end{bmatrix} \quad (4.2)$$

Flexible motion can be derived as

$$M_{fr} \ddot{q}_r + M_{ff} \ddot{q}_f + K_{ff} q_f = Q_f \quad (4.3.a)$$

or

$$M_{ff} \ddot{q}_f + K_{ff} q_f = Q_f - M_{fr} \ddot{q}_r \quad (4.3.b)$$

where \ddot{q}_r are chosen from desired the acceleration path function.

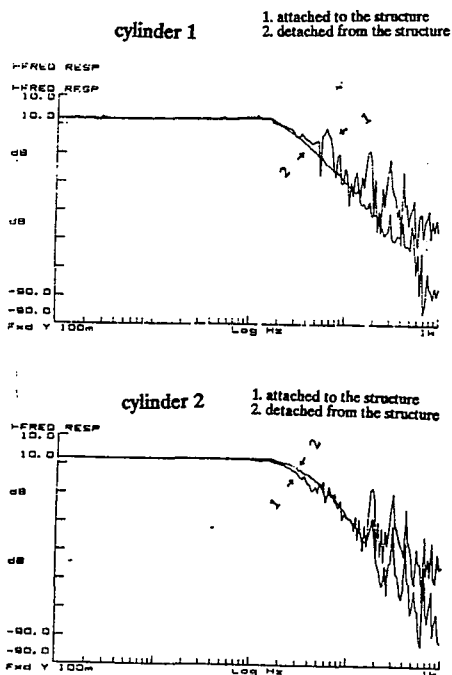


Figure 4.1
Closed loop Bode plots

A variety of movements of the manipulator were used for verification. First, a single link was moved while holding the other link fixed. Then both links were moved simultaneously. The desired path of the links was sinusoidal in joint space. All of the tests were made with no payload because the first two system modes are more clearly separated with no loading. Both the amplitude and the frequency of the movements were varied in order to compare the experimental results with the predicted results. During the movements of the manipulator, the following measurements were made:

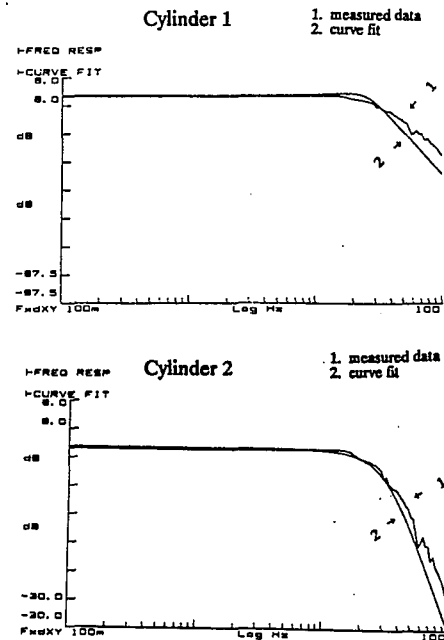


Figure 4.2
3rd order curve fit of actual Bode plot

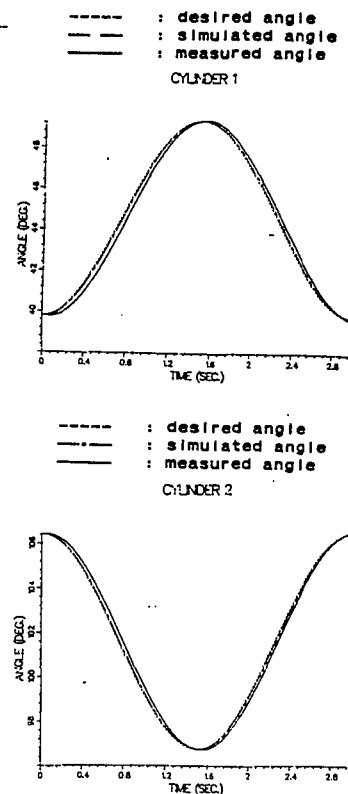


Figure 4.3
Time response of the rigid body motion

1. Joint angles
2. Displacement of the cylinders (LVDT)
3. Differential pressure in the cylinder
4. Strain at the midpoint in each link

Due to the high gains required to increase the closed loop bandwidth, small disturbances had a large effect on the movement and measurements made. The analytical model assumes that there are no disturbances and that the structure is ideal. This is never the case with actual systems. The effect of each disturbance can be seen in the measurement of the bending strain. In this section, these discrepancies will be examined and their causes explained. The agreement of the model with the experimental results will also be examined.

To compare the actual movements with the simulated results, the primary measurements were the displacements of the cylinders and the strain measurements. The displacement measurements show the rigid body motion. The strain measurements show the flexible motion. Figure 4.4 shows a typical plot of the experimental measurement of strain in the lower link in which the effects of the flexible motion can be clearly seen.

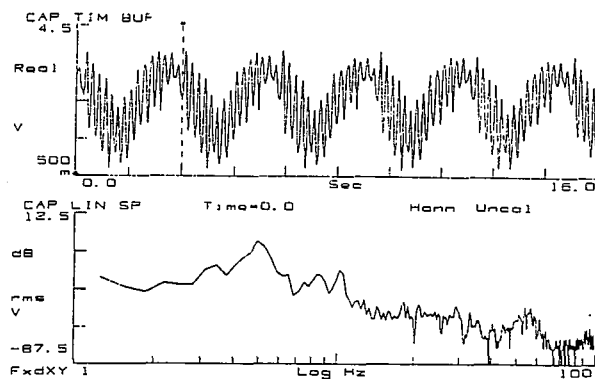


Figure 4.4
Typical strain measurement in lower beam

In the following figures, a comparison of the results is shown for one cycle of motion. As might be expected, there were some discrepancies between actual and predicted results. However, the results showed similar trends and the discrepancies can be explained. Generally, the measured strain in the lower link matches the strain predicted. The results for the upper link do not match as closely because there are no simple theoretical boundary conditions that match the actual boundary conditions and because only two mode shapes are used. Figure 4.5 shows the strain in links when both links are moving.

In Figures 4.5a and 4.5b the strain in the lower link has the same general shape in both the experimental and theoretical results except for the disturbance at the peak of the movement. Both plots show that there is little damping in the lower link and that the vibration of the upper link has little effect on the vibration of the lower link. The disturbance in the measured strain was found to be caused by a worn bearing in the actuator cross support (θ_2 in Fig. 2.1). A jump in the strain measurements occurs every time the upper link changes direction. The jump is most clearly seen in the strain of the lower link when only the upper link is in motion, as is shown in Figure 4.6a, but is noticeable in every measurement. For example, Figure 4.5c shows a disturbance in the strain in the upper beam, at the same time that the disturbance occurs in the lower beam.

Figure 4.6 shows the strain measurements in the upper and lower links when only the upper link is moving. The first

discrepancy noticed is the jump in strain. Again, this was caused by the mechanical looseness in the actuator cross support. The similarity in the strain in the lower link, Figures 4.6a and 4.6b, is that both plots show little damping for the cycle of motion. Figure 4.6a shows more effect of the upper link's vibration than is predicted by the model, Fig. 4.6b. Figures 4.6c and 4.6d show the strain in the upper beam. The measured strain in the upper beam clearly shows the effect of two disturbances. The first disturbance has already been discussed. The second disturbance, point A in Figure 4.6c, occurs at the maximum velocity and zero acceleration. A pure inertia load would display lost motion (backlash) at this point in the motion cycle. The reversal of differential pressure in the cylinder is another possible explanation for the observed disturbance. The seal deflection can result in behavior similar to backlash. Fig. 4.7 shows the control signal, strain, desired cylinder position, and actual cylinder position for θ_2 motions. The timing of the events is more obvious on this plot. Measurements of the differential pressure in the cylinder show that there is a 150 psi pressure variation concurrent with the disturbance. This may seem insignificant, but experience with the structure has shown that any disturbance seems large because of the large size of the structure and the use of large amplification of the strain signals. Without the effect of these two disturbances, the decrement of the amplitude of the strain in the experimental results would match fairly well with the decrement of the predicted strain as shown in Fig 4.6c and 4.6d.

It is obvious from these experiments that the experimental results do not exactly match the theoretical results. However, there is enough agreement in the general trend of the vibrations and their amplitudes when the disturbances are ignored to realize that the experimental results and the theoretical results can match if further efforts are made to reduce the disturbance in the experimental data.

5. Acknowledgement

This work was supported through grant number NAG 1-623 of the National Aeronautics and Space Administration and through the Computer Integrated Manufacturing Systems program at Georgia Institute of Technology.

REFERENCES

- (1) Asada, H., and Youcef-Toumi, K., "Analysis and Design of a Direct-Drive Arm with a Five-Bar-Link Parallel Drive Mechanism," *ASME Journal of Dynamic Systems, Measurement, and Control*, 106, Sept. 1984, pp. 225-230.
- (2) Megahed, S., and Renaud, M., "Dynamic Modelling of Robot Manipulators Containing Closed Kinematic Chains," *Advanced Software in Robotics*, Liege, Belgium, May, 1984, pp. 147-159.
- (3) Luh, J.Y.S., and Zheng, Y.F., "Computation of Input Generalized Forces for Robots with Closed Kinematic Chain Mechanism," *IEEE Journal of Robotics and Automation*, 1(2), June 1985, pp. 95-103.
- (4) Chung, Y.C., Book, W.J., and Lu, S.S., "Modeling and Optimal Control of Lightweight Bracing Manipulator," Internal Report, School of Mechanical Engineering, Georgia Tech, May, 1986.
- (5) Nikravesh, P.E., "Some Methods for Dynamic Analysis of Constrained Mechanical System: A Survey," *Computer Aided Analysis and Optimization of Mechanical System Dynamics*, E.J., Haug, ed., Springer-Verlag, Heidelberg, West Germany, 1984.
- (6) Wehage, R.A. and Haug, E.J., "Generalized Coordinate Partitioning for Dimension Reduction in Analysis of Constrained Dynamic Systems," *ASME Journal of Mechanical Design*, 104, (1), 1982, pp. 247-255.

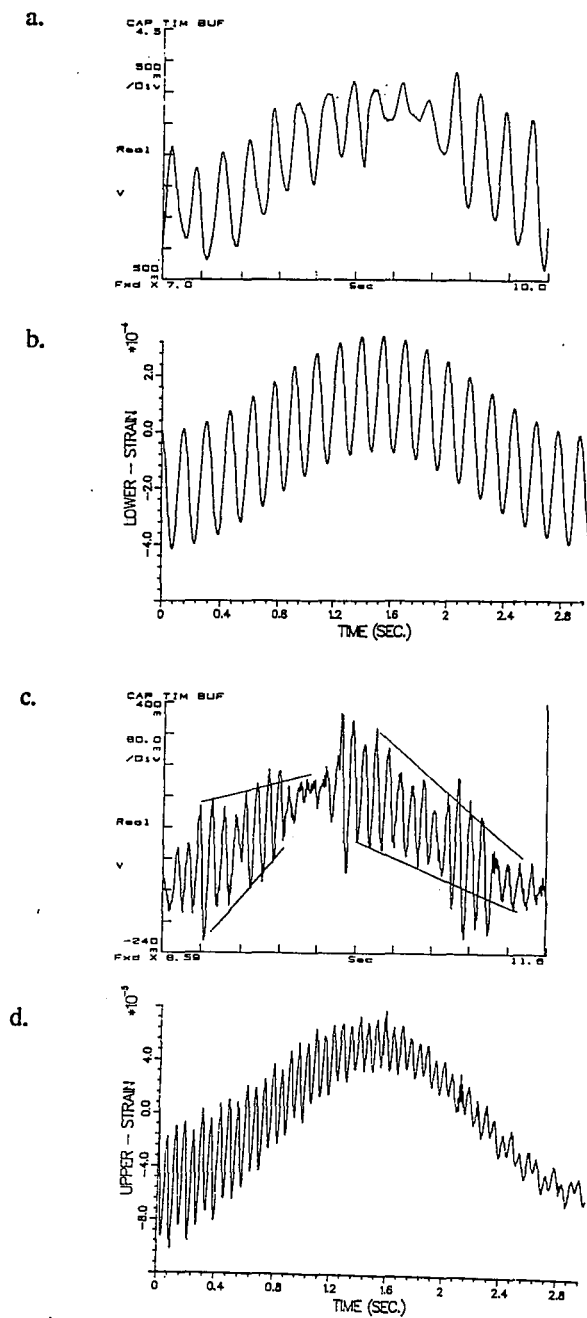


Figure 4.5
Strain of each link when both links moving

- a. Measured strain in lower link
- b. Simulated strain in lower link
- c. Measured strain in upper link
- d. Simulated strain in upper link

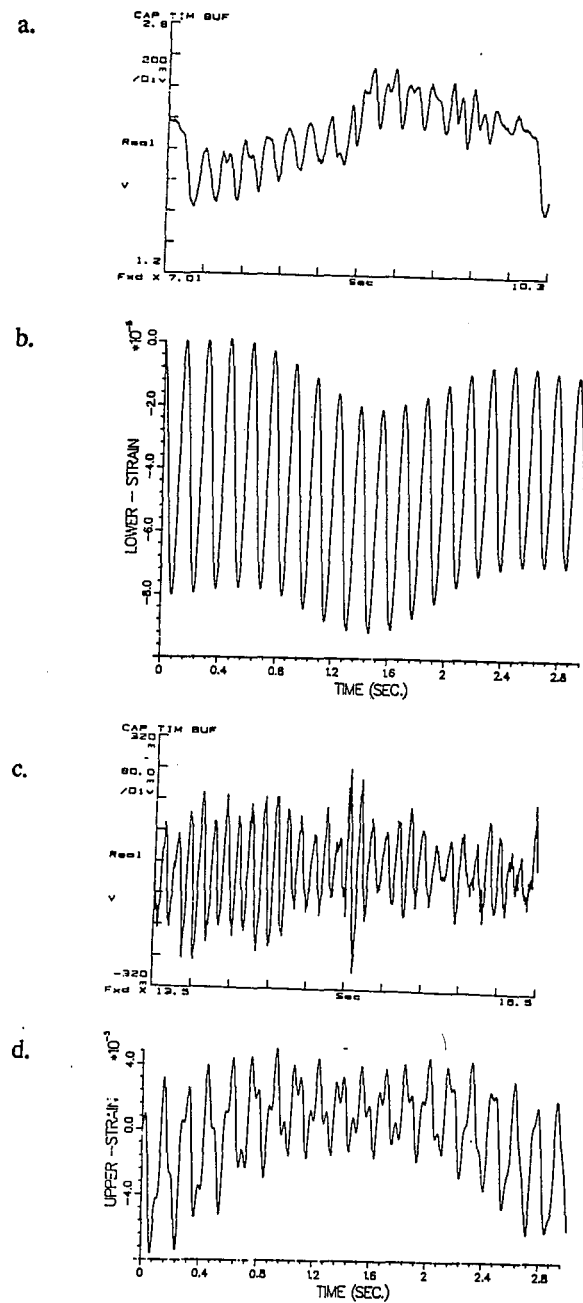


Figure 4.6
Strain of each link when lower links moving

- a. Measured strain in lower link
- b. Simulated strain in lower link
- c. Measured strain in upper link
- d. Simulated strain in upper link

(7) Mani, N.K., Haug, E.J., and Atkinson, K.E., "Application of Singular Value Decomposition for Analysis of Mechanical System Dynamics," ASME Journal of Mechanisms, Transmissions, and Automation in Design, 107, March 1985, pp. 82-87.

(8) Singh, R.P., and Linkins, P.W., "Singular Value Decomposition for Constrained Dynamic Systems," ASME Journal of Applied Mechanics, 52(4), Dec. 1985, pp. 943-948.

(9) Kim, S.S., Vanderploeg, M.J., "QR Decomposition for State Space Representation of Constrained Mechanical Dynamic Systems," ASME Journal of Mechanisms, Transmissions, and Automation in Design, 108, June 1986, pp. 183-188.

(10) Klema, V.C., and Laub, A.J., "The Singular Value Decomposition; Its Computation and Some Applications," IEEE Transaction on Automatic Control, 25, 1980, pp. 164-176.

(11) SMP Reference Manual, Inference Corporation, 1983

(12) Huggins, J.D., Kwon, D.S., Lee, J.W., and Book, W.J., "Alternative Modeling and Verification Techniques for A Large Flexible Arm," Applied Motion Control Conference, 1987, pp. 157-164.

(13) Merritt, H.E., Hydraulic Control Systems, John Wiley & Sons, Inc. 1967

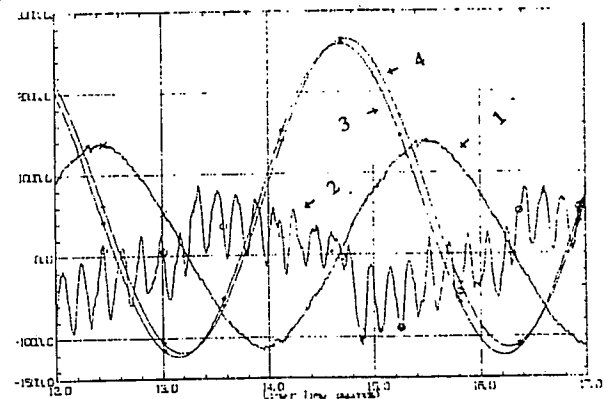


Figure 4.7
The composite plot of
control signal, strain, and positions

1. control signal
2. upper link strain
3. desired cylinder position
4. actual cylinder position